



A fully-conjugated covalent organic framework-derived carbon supporting ultra-close single atom sites for ORR

Shuai Yang ^{a,b,c,1}, Xuewen Li ^{a,b,c,1}, Tingyuan Tan ^{a,b,c,1}, Jianing Mao ^{a,b,c}, Qing Xu ^{c,d,*}, Minghao Liu ^d, Qiyang Miao ^d, BingBao Mei ^b, Panzhe Qiao ^b, Songqi Gu ^b, Fanfei Sun ^{b,c}, Jingyuan Ma ^{b,c}, Gaofeng Zeng ^{c,d,*}, Zheng Jiang ^{a,b,c,*}

^a Shanghai Institute of Applied Physics, Chinese Academy of Science, Shanghai 201210, PR China

^b Shanghai Synchrotron Radiation Facility, Zhangjiang Lab, Shanghai Advanced Research Institute, Chinese Academy of Science, Shanghai 201210, PR China

^c University of Chinese Academy of Sciences, Beijing 100049, PR China

^d CAS Key Laboratory of Low-Carbon Conversion Science and Engineering, Shanghai Advanced Research Institute, Chinese Academy of Science, Shanghai 201210, PR China



ARTICLE INFO

Keywords:

Derived covalent organic framework
Oxygen reduction
Single atom catalysis

ABSTRACT

Covalent organic frameworks linked by C=C bonds have gained great attention for various application, and their fully conjugated skeletons were potentially converted into two-dimensional (2D) carbons. Herein, we described a novel strategy to fabricate 2D carbon nanorods from a sp^2 carbon linked COF, which had a high surface area of $804.8 \text{ m}^2 \text{ g}^{-1}$. The one-dimensional channels confined the Fe ions during pyrolysis, which facilitated to form ultra-close atomic sites. The resulting catalyst displayed high catalytic activity towards oxygen reduction reaction, with a half-wave potential of 0.82 V and a mass activity of $4087.9 \text{ mA mg}^{-1}$ at 0.7 V versus RHE, which were high than those of Pt/C (0.81 V and 126.3 mA mg^{-1}). The theoretical calculation revealed the close FeN_4 sites achieved a lower $^*{\text{OH}}$ adsorption energy than isolated FeN_4 sites. This work provides a new insight into developing single atom catalysts from COFs.

1. Introduction

Covalent organic frameworks, as a class of porous polymers, are constructed by designable building blocks through covalent bonds [1–6]. Owing to their controllable skeletons and porosities, COFs have shown various application in gas absorption, ionic conduction, heterogeneous catalysis, membrane science, and energy storage and conversion [7–13]. Recently, the COFs linked by C=C bonds are getting more attention, because of these ultra-high chemical and thermal stability [14–19]. The C=C bonds of COFs facilitate electron transport along the frameworks, which render them used in semiconductors for photocatalysis and luminescence [20–30]. Importantly, their fully conjugated frameworks are similar to that of graphene, thus which are potentially used as the precursors for fabricating two-dimensionally carbon [14,15].

Oxygen reduction reaction (ORR) is important in electrochemical energy storage and conversion devices, including metal-air batteries and

fuel cells [31–34]. Pt based catalysts are demonstrated as the most active catalysts, nevertheless their high-cost and weak-durability are serious issues for further applications [35,36]. Many strategies have been adopted to develop highly efficient and stable catalysts for ORR. Given that high atom utilization efficiency and superior chemical stability, carbon-based single-atom catalysts were considered as the candidates to replace Pt/C in ORR [37–43]. Till now, different carbons including graphene, carbon nanotubes and metal organic frameworks-derived carbons are used as the supports to anchor metal atoms [44–48]. In 2020, Li et al. have first demonstrated RT-COF-derived carbon for immobilizing Fe ions for ORR [49]. And Xu et al. develop 3D-COF-derived carbons to support Co atoms [50]. More recently, Zhou et al. have used Tppa-COF to immobilize atomic Fe sites [51]. However, all of these metal ions in the catalysts were isolated atomic sites. And recent studies have demonstrated that atom sites with ultraclose distance such as dual-metal atoms could further enhance the catalytic activity and

* Corresponding authors.

** Corresponding author at: Shanghai Institute of Applied Physics, Chinese Academy of Science, Shanghai 201210, PR China.

E-mail addresses: xuqing@sari.ac.cn (Q. Xu), zenggf@sari.ac.cn (G. Zeng), jiangzheng@sinap.ac.cn (Z. Jiang).

¹ These authors contributed equally to this work.

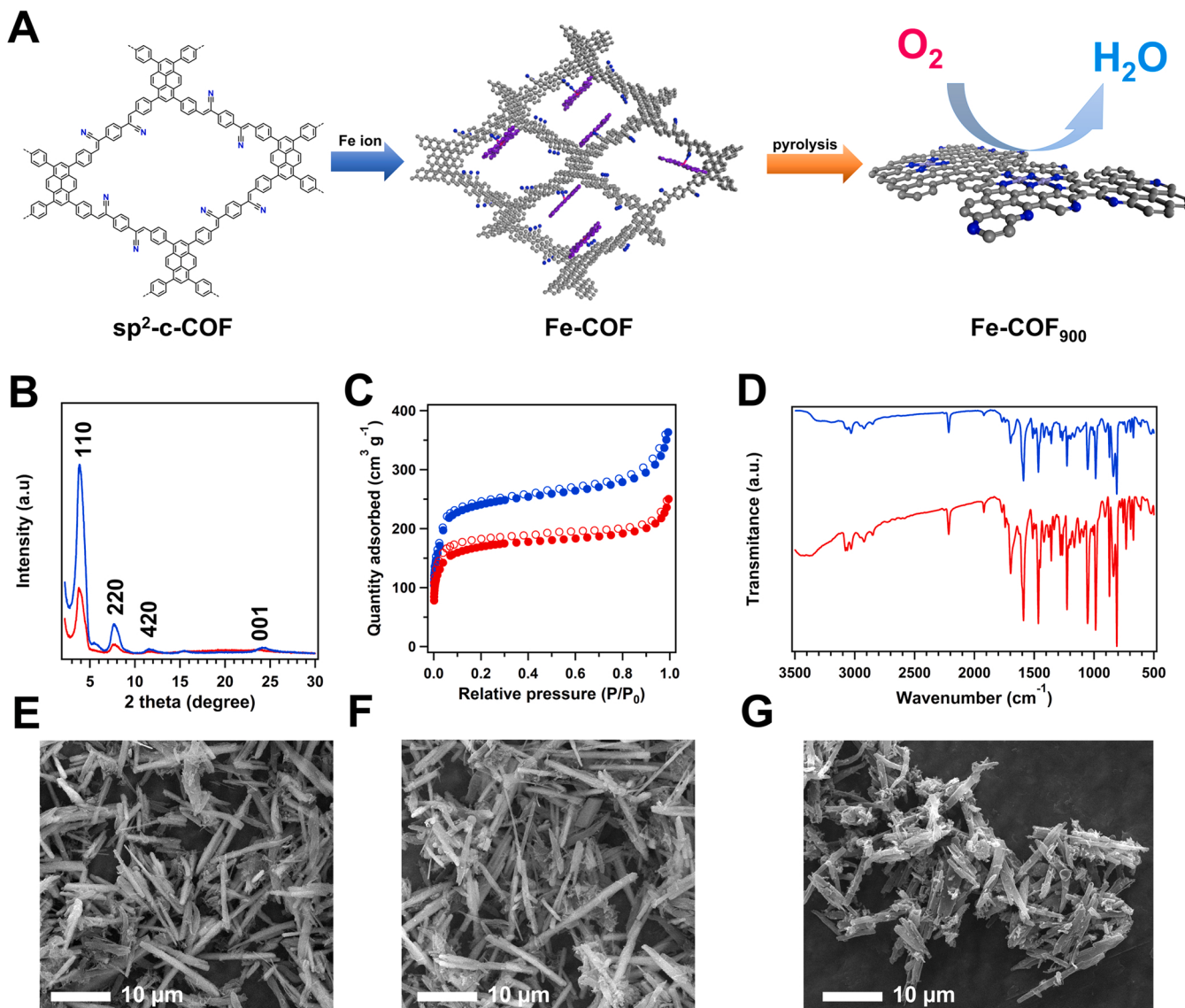


Fig. 1. (A) Synthesis of Fe-COF₉₀₀ from sp²-c-COF. (B) PXRD patterns, (C) Nitrogen sorption isotherm of samples at 77 K, and (D) Fourier transform infrared spectra of sp²-c-COF (blue) and Fe-COF (red). SEM images of sp²-c-COF (E), Fe-COF (F) and Fe-COF₉₀₀(G).

selectivity in various catalytic conversion reactions [52–58]. Herein, we have first developed 2D carbon from a fully conjugated framework to support ultra-close atomic Fe sites to catalyze ORR.

2. Experimental section (details at [supporting materials](#))

2.1. Synthesis of Fe-COF₉₀₀

The COF precursor (sp²-c-COF) was synthesized from 1,3,6,8-tetrakis (4-formylphenyl) pyrene (TFPPy) and 2,2'-(1,4-phenylene) diacetone nitrile (PDAN) in 1,4-dioxane with KOH (4 M) as catalyst at 90 °C for 3 days according to previous reports [15,16]. The Fe²⁺ ions (Fe-porphyrin) were absorbed on the surface and the pores of the frameworks to yield Fe-COF. Typically, the porphyrin molecules were adsorbed on the C≡N sites in 1D channels of sp²-c-COF via coordination effect [59,60]. The sp²-c-COF and Fe-COF were then annealed at 900 °C for 2 h under N₂ to prepare COF₉₀₀ and Fe-COF₉₀₀, respectively (Fig. 1A). COFs layers are stacked in edge-on direction or face-on direction. After thermal treatment, the edge-on layers were converted into standing carbon layers. And these standing carbon layers play more active roles in ORR [45]. In addition, the 1D channel of the COF confined the porphyrin

molecules migration along the pore channels after pyrolysis, which facilitated forming the planar-like ultra-close Fe-N₄ [61].

3. Results and discussion

3.1. Characterizations of catalysts

The powder X-ray diffraction measurement (PXRD) and nitrogen sorption isotherms were conducted to investigate the crystallinity and porosity of prepared sp²-c-COF and Fe-COF. The peaks at 3.8°, 7.6°, 11.6° and 24.2° were identified for sp²-c-COF in PXRD patterns, which were from 110, 220, 420 and 001 facets (Fig. 1B, blue curve). With absorbing Fe ions, these peaks were also clearly observed, suggesting its crystallinity was well maintained (Fig. 1B, red curve). The N₂ adsorption curves at 77 K revealed the Brunauer-Emmett-Teller (BET) surface area of the sp²-c-COF was 610.8 m² g⁻¹, with a pore volume of 0.61 cm³ g⁻¹. And Fe-COF has a lower BET surface area of 418.1 m² g⁻¹ (Fig. 1C), with a corresponding pore volume of 0.45 cm³ g⁻¹. The decreased surface area and lower pore volume were due to the Fe²⁺ was loaded into the pores and on the surface of the COF.

The chemical structure of the sp²-c-COF and Fe-COF were first

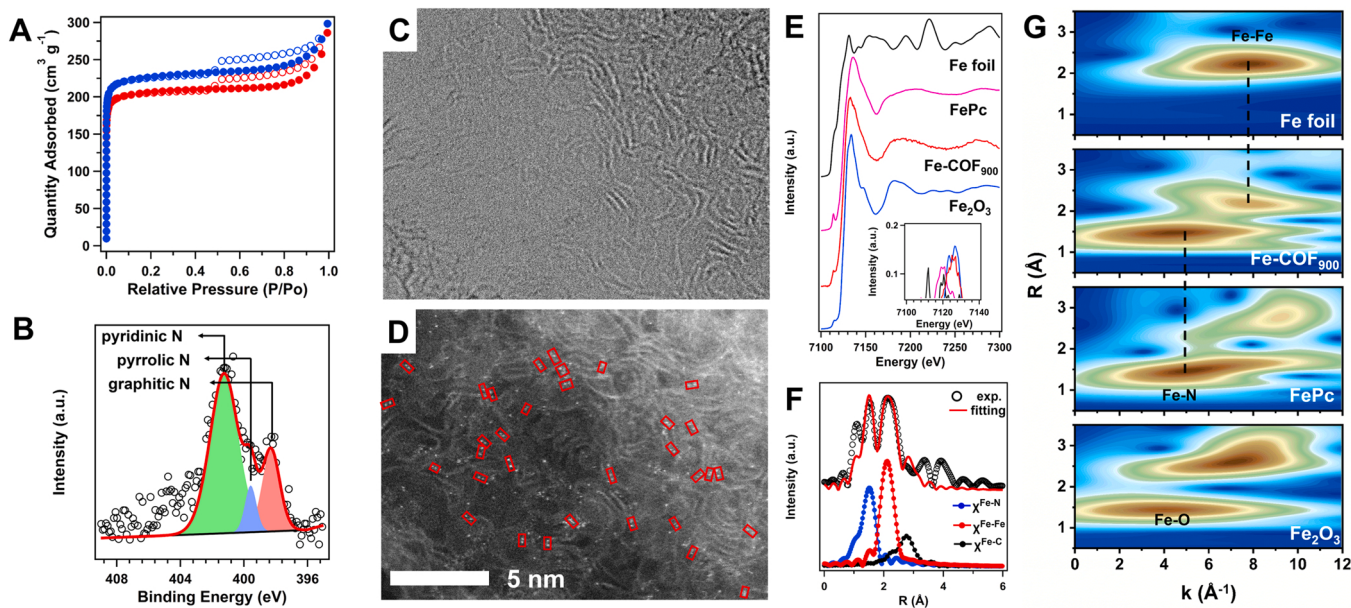


Fig. 2. (A) Nitrogen sorption isotherm of COF₉₀₀ (blue) and Fe-COF₉₀₀ (red) at 77 K. (B) High-resolution XPS N 1 s spectrum of Fe-COF₉₀₀. (C) and (D) Atomic-resolution HAADF-STEM images. (E) XANES spectra of samples and corresponding first derivative spectra (insert pattern). (F) The Fe K-edge k^3 -weighted Fourier transform spectra from EXAFS of Fe-COF₉₀₀. The black dots are experimental results, and the red line are best-fit curves for $R = 1\text{--}3.0\text{ \AA}$, using corresponding $k^3\chi(k)$ functions in $k = 3.0\text{--}11.9\text{ \AA}^{-1}$. The χ signals are the three-body backscattering paths of Fe-N, Fe-Fe and Fe-C. (G) Wavelet transform contour spectra for the k^2 -weighted EXAFS data.

investigated by Fourier transform infrared spectroscopy (FT IR). The typical peak at $\sim 2220\text{ cm}^{-1}$ was found for sp^2 -c-COF, which was due to the $\text{C}\equiv\text{N}$ vibration band (Fig. 1D, blue curve). And the intensity of the peak at 2720 cm^{-1} displayed decreased, which was assigned to the C-H stretching vibration of the aldehyde units. The solid ^{13}C cross-polarization/magic-angle spinning solid-state nuclear magnetic resonance (CP/MAS NMR) was conducted to exploring the chemical structure. The peak at ~ 110 ppm was assigned to $\text{C}\equiv\text{N}$, while the peak at ~ 118 ppm correspond to the CN-substituted vinylene linkages (Fig. S1). Thus, the sp^2 -c-COF has successfully synthesized. With loading Fe ions, these peaks exhibited slight changes, suggesting the frameworks were well maintained (Fig. 1D, red curve).

The chemical structure of sp^2 -c-COF and Fe-COF were then studied by XPS spectrum. The C 1 s and N 1 s signs were clearly identified for both COFs. And the N contents for sp^2 -c-COF and Fe-COF were 3.32 wt% and 5.34 wt%, respectively (Fig. S2 and S3). The inductively coupled plasma atomic emission spectrometer (ICP-AES) showed the Fe content in Fe-COF was only 0.08 wt%.

We then investigated their morphologies scanning electron microscopy (SEM) images and transmission electron microscopy (TEM) images. The SEM images revealed that sp^2 -c-COF and Fe-COF was in uniformly ribbon-sharp (Figs. 1E, 1F and S4). The energy dispersive spectroscopy (EDS) mapping images showed all the elements were uniformly distribution along the frameworks (Fig. S5 and S6). The ribbon size for Fe-COF was as same as that of sp^2 -c-COF. The thermal stability of the prepared COFs was studied. According to the TGA curves, sp^2 -c-COF and Fe-COF were stable before 320 °C, and the weight left were about 70% at 800 °C under N₂ atmosphere (Fig. S7).

The sp^2 -c-COF and Fe-COF were then pyrolyzed under N₂ to obtain the COF₉₀₀ and Fe-COF₉₀₀. The PXRD pattern of COF₉₀₀ and Fe-COF₉₀₀ showed the peaks at 20.9° and 44.0°, which were from (002) and (100) facets of the carbon (Fig. S8). And no other peaks were observed for Fe-COF₉₀₀, indicating no aggregated metal particles in the carbon. The COF₉₀₀ and Fe-COF₉₀₀ conformed between type-I and type-II absorption, suggesting their hierarchical pores. The corresponding BET surface areas for COF₉₀₀ and Fe-COF₉₀₀ were 804.8 and 714.3 m² g⁻¹, with total pore volumes of 0.46 and 0.30 cm³ g⁻¹ (Fig. 2A), respectively. And the pore

size distribution curves showed the microporous volumes for COF₉₀₀ and Fe-COF₉₀₀ were 0.33 and 0.26 cm³ g⁻¹ (Fig. S9 and S10).

The chemical properties of the carbons were then studied by XPS spectra. The contents for N of COF₉₀₀ and Fe-COF₉₀₀ were 1.41 wt% and 1.43 wt%, respectively. And XPS N 1 s spectra of COF₉₀₀ and Fe-COF₉₀₀ can be deconvoluted into three types of nitrogen: pyridinic N (N1) at $\sim 398\text{ eV}$, pyrrolic N (N2) at $\sim 399\text{ eV}$, and graphitic N (N3) at $\sim 401\text{ eV}$. And the relative contents for pyridinic N (N1), pyrrolic N (N2) and graphitic N (N3) of COF₉₀₀ were 36.7 at%, 0 and 63.3 at%, respectively (Fig. S11). The high-resolution N 1 s spectra for Fe-COF₉₀₀ showed the relative content for N1, N2 and N3 were 28.3 at%, 55.6 at%, and 16.1 at % (Fig. 2B). However, the spectra for Fe in Fe-COF₉₀₀ signal was too weak to distinguish. The content for Fe was determined by ICP-AES, with a low value of 0.15 wt%.

In addition, we have used Raman spectrum to study the defects of prepared carbons (Fig. S12). The peaks at 1337 cm^{-1} (D band) and 1583 cm^{-1} (G band) were from the carbon defects (such as sp^3 -carbon disorder in graphene basal planes) and sp^2 carbons, respectively. The $I_{\text{D}}/I_{\text{G}}$ ratio between them were 1.00 and 1.00, suggesting the defects of the carbon were well retained after loading Fe element on the surface.

The SEM images, TEM and HR-TEM images confirmed the 2D morphologies of COF₉₀₀ and Fe-COF₉₀₀ (Fig. S13–S16). The micro-structure of carbons was further analyzed by HR-TEM images. Lots of nano-rods were observed in different direction on the surface of COF₉₀₀. And these standing carbons were also identified exposed on the surface of the 2D carbons (Fig. 2C). High-angle annular dark-field scanning transmission electron microscopy (HAADF-STEM) images showed bright dots are clearly identified on the surface of standing carbons (Fig. 2D), which were corresponding to Fe atoms. The large number of pair bright dots were clearly observed, implied the distance of Fe atoms are closed.

Rely on advanced synchrotron radiation facility, X-ray absorption spectroscopy (XAS) measurements is powerful to identify the local coordination structure and the chemical state of Fe atoms. As shown in Fe K-edge X-ray absorption near-edge structure (XANES) spectra (Fig. 2E), the white line peaks are clear observed, which correspond to transition from 1 s core-electron to 4p orbital. It is directly recognized the outline of Fe-COF₉₀₀ was similar to that of Iron phthalocyanine (FePc), meaning

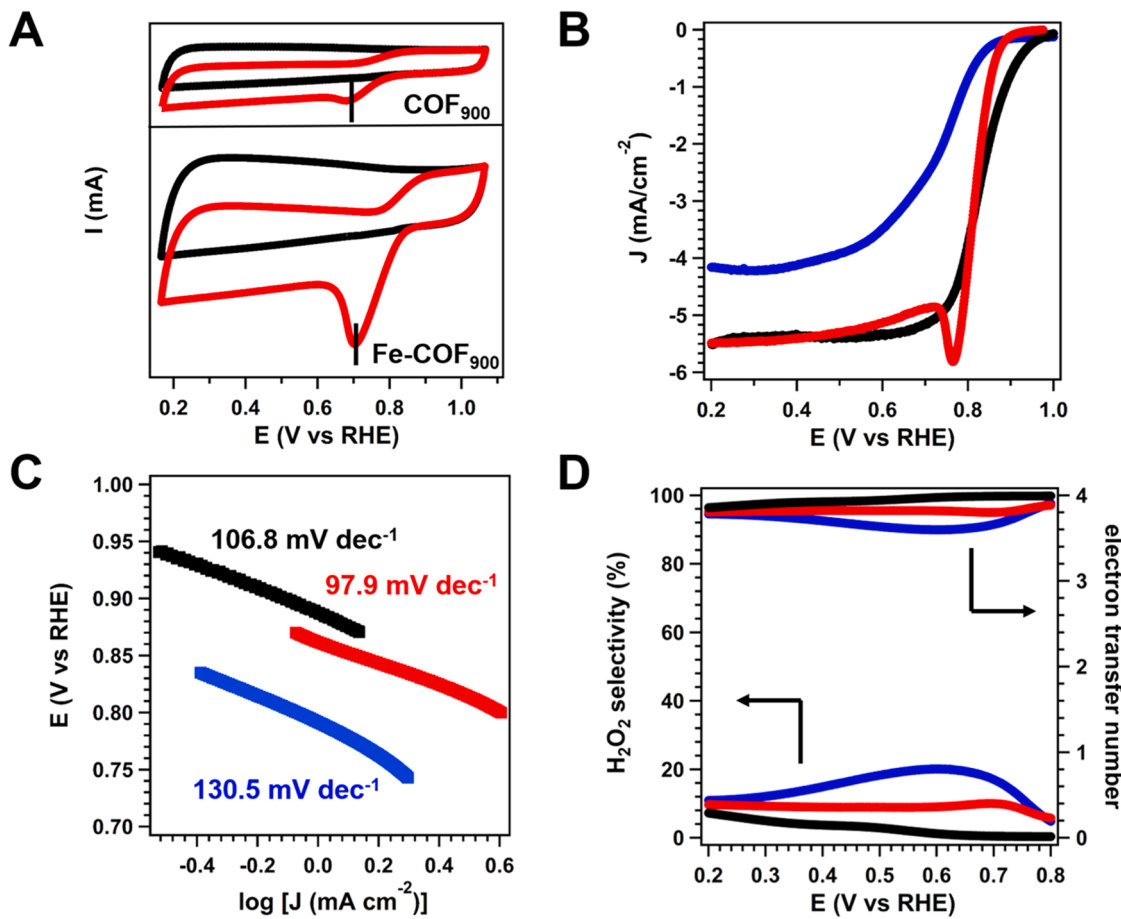


Fig. 3. (A) Cyclic voltammetry (CV) curves in O_2 -saturated (red) and N_2 -saturated (black) of COF_{900} and $Fe-COF_{900}$. (B) LSV curves, (C) the Tafel plots and (D) number (n) of electrons transferred, and H_2O_2 yield plots calculated from the RRDE measurements for COF_{900} (blue), $Fe-COF_{900}$ (red), and 20 wt%Pt/C (black).

a similar photoelectron multiple scattering. The pre-edge peaks were caused by $1s \rightarrow 3d/4p$ transition, that implied the Fe atoms with a low symmetry at first shell and un-occupied d orbital. For simply quantification of the pre-edge peaks, we caculated the integral area of each peaks (Fig. S17), the value of $Fe-COF_{900}$ (0.13) is higher than Fe_2O_3 (0.05) and lower than $FePc$ (0.21). [62,63] The average symmetry of each Fe atoms in $Fe-COF_{900}$ is higher than that of $Fe-O$ octahedron and lower than that of $Fe-N$ quadrangle. The absorption edge of $Fe-COF_{900}$ was close to Fe_2O_3 and upper than $FePc$, indicating $Fe-COF_{900}$ with a slightly lower average oxidation state than Fe_2O_3 (insert figure in Fig. 2E). These results claimed that the atomic structure of $Fe-COF_{900}$ tends to modified $Fe-NC$.

For further exploration, extend X-ray absorption fine structure (XAFS) was employed to acquire local configuration information surrounding Fe centers. Fourier transforms of the EXAFS spectra expressed radical structure in real space (Fig. S18). $Fe-COF_{900}$ firstly exhibits similar Fe-N coordination with a peak at about 1.53 Å, which close to Fe-N peak in $FePc$ (1.54 Å) and more higher than Fe-O (1.44 Å). Another main peak located at 2.13 Å seems more complicated, which dramatically lower than Fe-O-Fe (2.59 Å). This broad peak looks like influenced by the Fe-Fe (2.21 Å) and a little satellite peak (2.79 Å) points to Fe-C (2.50 Å). Combined with the synthesis process and above characterization, we reasonably attributed this shell to Fe-C and Fe-Fe coordination. For getting separating backscattering atoms' resolution in the k-space and radial distance simultaneously, the wavelet transform (WT) of K-edge EXAFS oscillations was conducted (Fig. 2G). The intensity maximum of each samples possess different coordinates (k , R), whose location is mainly connected with the scattering function depended on the atomic number. The two centers located at 5 Å⁻¹ and 8 Å⁻¹ of Fe-

COF_{900} were aligned with the first center of $FePc$ and main center of Fe foil, indicating the scattering contribution of N/O and Fe, respectively. To quantitatively reveal the detail coordination information, least-squares EXAFS curve-fitting analysis was employed. In Fig. 3F, the fitting results contains three path Fe-N, Fe-Fe and Fe-C (or N), and corresponding coordination number is 4.0, 1.8 and 8.0, atomic distance is 1.98 Å, 2.52 Å and 3.34 Å (Table S1). These results demonstrated the Fe structures equipped Fe-N₄ and a larger Fe-Fe linkage. The Fe-Fe distance (2.52 Å) much lower than the graphite layer spacing (~3.3 Å), we can exclude the situation of Fe-Fe axial bonding. The atomic-resolution HAADF-STEM images showed the large number of pair dots is about the same brightness (Fig. 2D), that implied the planar Fe sites coupling is mainly existed form. Therefore, majority catalytic sites configuration can reasonably deduced: the two Fe atoms shared the adjacent two N atoms, and formed the ultra-close single atom sites structure.

Considering the standing carbons and ultra-close Fe-N₄ is active sites for catalyzing ORR, we investigate the catalytic behavior of COF_{900} and $Fe-COF_{900}$ in alkaline condition. As a control, the commercial Pt/C catalyst was tested in the same conditions. We measured the cyclic voltammetry (CV) in O_2 -saturated and N_2 -saturated 0.1 M KOH at a scan rate of 50 mV s⁻¹, respectively (Fig. 3A). A well-defined cathodic peak at 0.70 V for $Fe-COF_{900}$ was shown under O_2 atmosphere, while no peaks were identified under N_2 condition, suggesting its catalytic ability. And the peak for COF_{900} was 0.68 V under O_2 -saturated atmosphere, negative than that of $Fe-COF_{900}$, indicating inferior activity of COF_{900} .

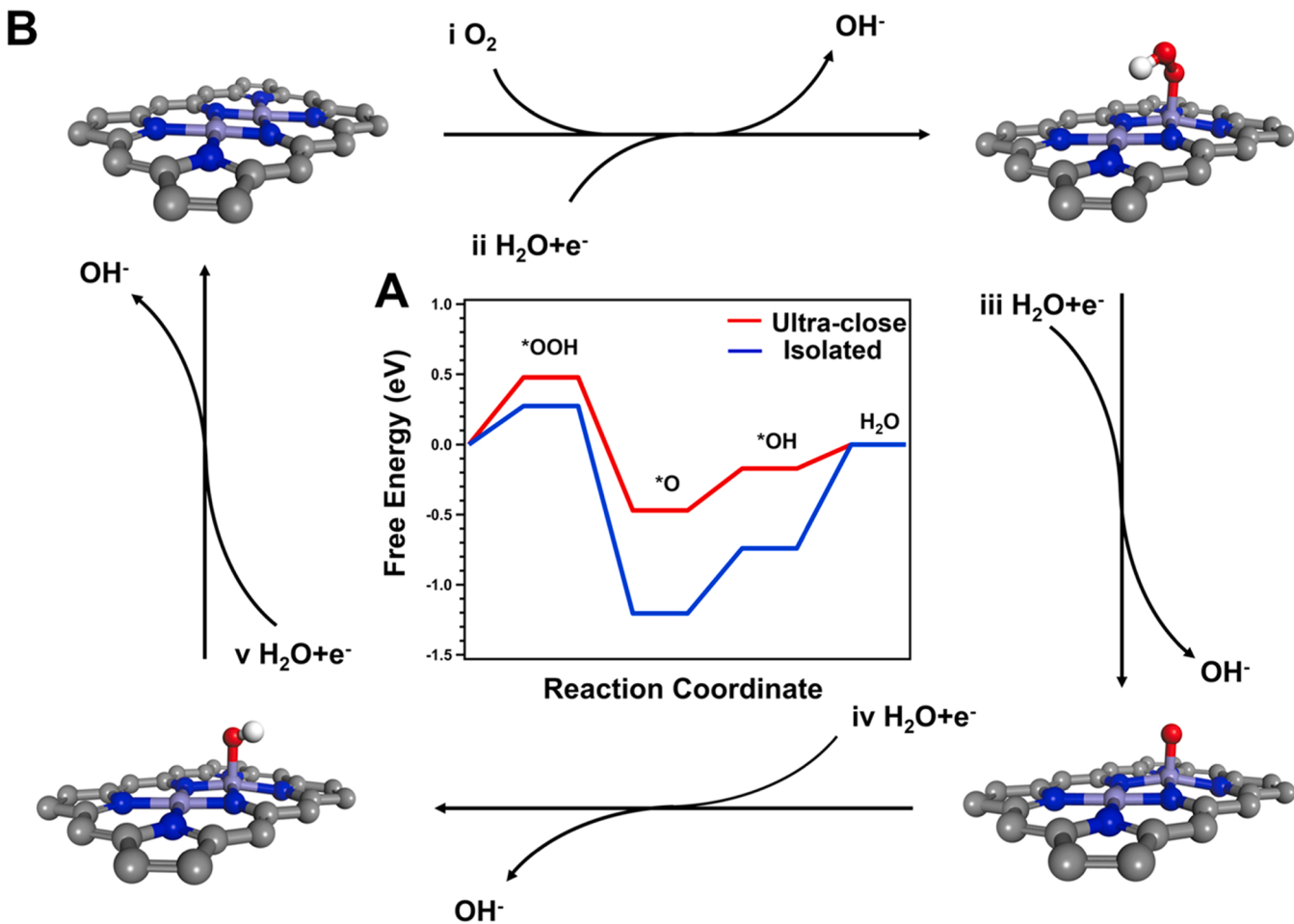


Fig. 4. The free energy diagram of active sites and its possible reaction pathway. (A) The free energy diagram of two kind of FeN_4 at different optimized adsorbed reaction sites at 1.23 V. (B) Favorable reaction pathway of ultra-close FeN_4 .

3.2. Electrocatalytic performance of catalysts

The ORR behaviors on COF₉₀₀ and Fe-COF₉₀₀ were further evaluated by the rotating disc electrode (RDE) measurement at 1600 rpm in O₂-saturated 0.1 M KOH solution. The 20 wt% Pt/C displayed the onset potential (E_o) and half-wave potential ($E_{1/2}$) for of 0.92 and 0.81 V, respectively (Fig. 3B, black curve). The onset potential (E_o) and half-wave potential ($E_{1/2}$) for COF₉₀₀ were 0.82 V and 0.74 V, with a limited current density (J_{lim}) of 4.15 mA cm⁻². With anchoring Fe atoms on the surface of the carbon, the Fe-COF₉₀₀ showed enhanced activity for ORR. The corresponding E_o and $E_{1/2}$ were 0.86 and 0.82 V, with a J_{lim} of 5.49 mA cm⁻², respectively. In addition, the corresponding mass activity were obtained according to the LSV curves, and the mass activity for Fe-COF₉₀₀ at 0.9, 0.8 and 0.7 V were 91.4, 3451.3, 4087.9 mA mg⁻², which were much high than those of Pt/C (19.22, 92.0 and 126.3 mA mg⁻²) at the same potentials, respectively. Moreover, we have investigated the kinetic behavior by Tafel slopes. The Tafel slope for Fe-COF₉₀₀ was 97.9 mV dec⁻¹ (Fig. 3 C, red curve), much smaller than that of Pt/C (106.8 mV dec⁻¹) and COF₉₀₀ (130.5 mV dec⁻¹), indicating its better kinetic behavior (Fig. 3 C, black curve). The corresponding kinetic current density (J_{kin}) of Fe-COF₉₀₀ was 18.4 mA cm⁻² at 0.75 V, which are higher than those of COF₉₀₀ (2.4 mA cm⁻²) and Pt/C (7.18 mA cm⁻²). The corresponding turnover frequency (TOF) of Fe-COF₉₀₀ achieved 4490 h⁻¹, over two orders of magnitude of that from Pt/C value (33.5 h⁻¹).

The H₂O-H₂O₂ selectivity of ORR on these catalysts were explored by the rotating ring-disk electrode (RRDE) measurements. The electron

transfer numbers for Fe-COF₉₀₀ were 3.80–3.88 in the range of 0.2–0.8 V (RHE), which were close to those of Pt/C (Fig. 3D) and higher than that COF₉₀₀ (3.59–3.81). The H₂O₂ yields over Fe-COF₉₀₀ are only 5.8–9.8% in the range of 0.2–0.8 V, much closer to that of Pt/C. Thus, Fe-COF₉₀₀ catalyzed ORR in 4e⁻ pathway.

The excellent long-term stability and chemical stability of the catalysts are also important for ORR. We have investigated the durability of Fe-COF₉₀₀ for 20 h. The current density was 96% of initial values, suggesting its good long-term stability (Fig. S19). And we have tested the chemical stability of Fe-COF₉₀₀ with addition MeOH to the aqueous solution. The current density was well retained after adding MeOH. Differently, the current density for Pt/C decreased obviously to 78% (Fig. S20).

To reveal the active sites of Fe-COF₉₀₀, we have conducted the SCN⁻ deactivated experiments. In alkaline condition, the Fe-COF₉₀₀ displayed the strong tolerance to the SCN⁻. $E_{1/2}$ displayed negative shift to 0.79 V, yet the corresponding platform J decreased to ~4 mA cm⁻² (Fig. S21). The decreased activity of Fe-COF₉₀₀ demonstrated the active sites were FeN_x in the catalyst.

3.3. Theoretical simulations

In order to acquiring reaction mechanism at atomic sight, the density functional theory (DFT) calculations were employed. We compared the ultra-close FeN_4 site and isolated FeN_4 site model in ORR process which involved multi-oxygen-intermediates (*OOH, *O, *OH) with an overpotential of 0.74 V. Isolated FeN_4 is more easily to adsorbed

intermediates (OOH^*), and the rate-determining step of reaction is at $^*\text{OH} \rightarrow \text{H}_2\text{O}$ (Fig. 4A, blue curve; Fig. S22), with an overpotential of 0.48 V. Differently, (Fig. 4A, red curve; Fig. 4B). And the rate-determining step for the catalyst with ultra-close active sites were from O_2 to OOH^* , with an overpotential of 0.48 V. Thus, the catalyst with ultra-close Fe-N sites displayed high activity than the catalyst constructed with isolated sites, that also demonstrated at experiment. (Fig. S23). The prepared isolated FeN_4 was investigated the catalytic performance towards ORR showed a lower activity than ultra-close sites.

4. Conclusions

In summary, we have first constructed two-dimensional carbons from a fully conjugated COF. The carbon enables to immobilize the pair Fe atoms on the surface, which catalyzed the ORR with high selectivity and activity. In addition, the catalyst showed extraordinary long-term stability and tolerance to methanol. And the DFT calculations confirmed the neighbored Fe sites optimized the $^*\text{OH}$ formation in ORR process. This work not only inspire more chances for the synthesis of atomic dispersed catalysts from COFs.

CRediT authorship contribution statement

Shuai Yang: Investigation, Data analysis, Validation, Writing – original draft. **Xuewen Li:** Investigation, Data analysis, Validation, Writing – original draft. **Qing Xu:** Investigation, Data analysis, Validation, Writing – original draft. **Tingyuan Tan:** Data analysis. **Jianing Mao:** Data analysis. **Minghao Liu:** Data analysis. **Qiyang Miao:** Data analysis. **Bing Bao Mei:** Data analysis. **Panzhe Qiao:** Data analysis. **Songqi Gu:** Data analysis. **Fanfei Sun:** Data analysis. **Jingyuan Ma:** Data analysis, Writing. **Qing Xu:** Validation, Writing - review & editing, Funding acquisition. **Gaofeng Zeng:** Validation, Writing – review & editing, Funding acquisition. **Zheng Jiang:** Validation, Writing – review & editing, Funding acquisition.

Declaration of Competing Interest

The authors declare that they have no known competing financial interests or personal relationships that could have appeared to influence the work reported in this paper.

Acknowledgements

Q. Xu acknowledges the financial support from Shanghai Pujiang Program (19PJ1410400). The authors acknowledge the financial support from the National Natural Science Foundation of China (NSFC Grant no. U1732267, 21972163, 22065107) and Innovation Academy for Green Manufacture, Chinese Academy of Sciences (No. IAGM2020C16). The authors would also thank beamline BL14W1 at SSRF for the beam time allocation and assistance.

Appendix A. Supporting information

Supplementary data associated with this article can be found in the online version at [doi:10.1016/j.apcatb.2022.121147](https://doi.org/10.1016/j.apcatb.2022.121147).

References

- [1] A.P. Côté, A.I. Benin, N.W. Ockwig, M. Keeffe, A.J. Matzger, O.M. Yaghi, Porous, crystalline, covalent organic frameworks, *Science* 310 (2005) 1166–1170.
- [2] C.S. Diercks, O.M. Yaghi, The atom, the molecule, and the covalent organic framework, *Science* 355 (2017) eaal1585.
- [3] S. Kandambeth, K. Dey, R. Banerjee, Covalent organic frameworks: chemistry beyond the structure, *J. Am. Chem. Soc.* 141 (2019) 1807–1822.
- [4] K. Geng, T. He, R. Liu, S. Dalapati, K.T. Tan, Z. Li, S. Tao, Y. Gong, Q. Jiang, D. Jiang, Covalent organic frameworks: design, synthesis, and functions, *Chem. Rev.* 120 (2020) 8814–8933.
- [5] X. Li, P. Yadav, K.P. Loh, Function-oriented synthesis of two-dimensional (2D) covalent organic frameworks – from 3D solids to 2D sheets, *Chem. Soc. Rev.* 49 (2020) 4835–4866.
- [6] Z. Li, T. He, Y. Gong, D. Jiang, Covalent organic frameworks: pore design and interface engineering, *Acc. Chem. Res.* 53 (2020) 1672–1685.
- [7] S. Lin, C.S. Diercks, Y.-B. Zhang, N. Kornienko, E.M. Nichols, Y. Zhao, A.R. Paris, D. Kim, P. Yang, O.M. Yaghi, C.J. Chang, Covalent organic frameworks comprising cobalt porphyrins for catalytic CO_2 reduction in water, *Science* 349 (2015) 1208–1213.
- [8] C. Montoro, D. Rodriguez-San-Miguel, E. Polo, R. Escudero-Cid, M.L. Ruiz-Gonzalez, J.A.R. Navarro, P. Ocon, F. Zamora, Ionic conductivity and potential application for fuel cell of a modified imine-based covalent organic framework, *J. Am. Chem. Soc.* 139 (2017) 10079–10086.
- [9] X. Zhao, P. Pachfule, S. Li, T. Langenhahn, M. Ye, C. Schlesiger, S. Praetz, J. Schmidt, A. Thomas, Macro/microporous covalent organic frameworks for efficient electrocatalysis, *J. Am. Chem. Soc.* 141 (2019) 6623–6630.
- [10] J. Li, X. Jing, Q. Li, S. Li, X. Gao, X. Feng, B. Wang, Bulk COFs and COF nanosheets for electrochemical energy storage and conversion, *Chem. Soc. Rev.* 49 (2020) 3565–3604.
- [11] M.S. Lohse, T. Bein, Covalent organic frameworks: structures, synthesis, and applications, *Adv. Funct. Mater.* 28 (2018), 1705553.
- [12] Y. Zang, C. Mi, R. Wang, H. Chen, P. Peng, Z. Xiang, S.Q. Zang, T.C.W. Mak, Pyrolysis-free synthesized catalyst towards acidic oxygen reduction by deprotonation, *Angew. Chem. Int. Ed.* 60 (2021) 20865–20871.
- [13] P. Peng, L. Shi, F. Huo, C. Mi, X. Wu, S. Zhang, Z. Xiang, A pyrolysis-free path toward superiorly catalytic nitrogen-coordinated single atom, *Sci. Adv.* 5 (2019) eaaw2322.
- [14] X. Zhuang, W. Zhao, F. Zhang, Y. Cao, F. Liu, S. Bi, X. Feng, A two-dimensional conjugated polymer framework with fully sp^2 -bonded carbon skeleton, *Polym. Chem.* 7 (2016) 4176–4181.
- [15] E. Jin, M. Asada, Q. Xu, S. Dalapati, A. Addicoat Matthew, A. Brady Michael, H. Xu, T. Nakamura, T. Heine, Q. Chen, D. Jiang, Two-dimensional sp^2 carbon-conjugated covalent organic frameworks, *Science* 357 (2017) 673–676.
- [16] M. Yu, R. Dong, X. Feng, Two-dimensional carbon-rich conjugated frameworks for electrochemical energy applications, *J. Am. Chem. Soc.* 142 (2020) 12903–12915.
- [17] E. Jin, J. Li, K. Geng, Q. Jiang, H. Xu, Q. Xu, D. Jiang, Designed synthesis of stable light-emitting two-dimensional sp^2 carbon-conjugated covalent organic frameworks, *Nat. Commun.* 9 (2018) 4143.
- [18] T. He, K. Geng, D. Jiang, All sp^2 carbon covalent organic frameworks, *Trends Chem.* 3 (2021) 431–444.
- [19] L. Zhai, S. Yang, X. Yang, W. Ye, J. Wang, W. Chen, Y. Guo, L. Mi, Z. Wu, C. Soutis, Q. Xu, Z. Jiang, Conjugated covalent organic frameworks as platinum nanoparticle supports for catalyzing the oxygen reduction reaction, *Chem. Mater.* 32 (2020) 9747–9752.
- [20] E. Jin, Z. Lan, Q. Jiang, K. Geng, G. Li, X. Wang, D. Jiang, 2D sp^2 carbon-conjugated covalent organic frameworks for photocatalytic hydrogen production from water, *Chem* 5 (2019) 1632–1647.
- [21] R. Chen, J.L. Shi, Y. Ma, G. Lin, X. Lang, C. Wang, Designed synthesis of a 2D porphyrin-based sp^2 carbon-conjugated covalent organic framework for heterogeneous photocatalysis, *Angew. Chem. Int. Ed.* 58 (2019) 6430–6434.
- [22] Y. Zhao, H. Liu, C. Wu, Z. Zhang, Q. Pan, F. Hu, R. Wang, P. Li, X. Huang, Z. Li, Fully conjugated two-dimensional sp^2 -carbon covalent organic frameworks as artificial photosystem I with high efficiency, *Angew. Chem. Int. Ed.* 58 (2019) 5376–5381.
- [23] Z. Fu, X. Wang, A.M. Gardner, X. Wang, S.Y. Chong, G. Neri, A.J. Cowan, L. Liu, X. Li, A. Vogel, R. Clowes, M. Bilton, L. Chen, R.S. Sprick, A.I. Cooper, A stable covalent organic framework for photocatalytic carbon dioxide reduction, *Chem. Sci.* 11 (2020) 543–550.
- [24] S. Xu, Y. Li, B.P. Biswal, M.A. Addicoat, S. Paasch, P. Imbrasas, S. Park, H. Shi, E. Brunner, M. Richter, S. Lenk, S. Reineke, X. Feng, Luminescent sp^2 -carbon-linked 2D conjugated polymers with high photostability, *Chem. Mater.* 32 (2020) 7985–7991.
- [25] S. Li, L. Li, Y. Li, L. Dai, C. Liu, Y. Liu, J. Li, J. Lv, P. Li, B. Wang, Fully conjugated donor-acceptor covalent organic frameworks for photocatalytic oxidative amine coupling and thioamide cyclization, *ACS Catal.* 10 (2020) 8717–8726.
- [26] J. Xu, Y. He, S. Bi, M. Wang, P. Yang, D. Wu, J. Wang, F. Zhang, An olefin-linked covalent organic framework as a flexible thin-film electrode for a high-performance micro-supercapacitor, *Angew. Chem. Int. Ed.* 58 (2019) 12065–12069.
- [27] J. Xu, C. Yang, S. Bi, W. Wang, Y. He, D. Wu, Q. Liang, X. Wang, F. Zhang, Vinylene-linked covalent organic frameworks (COFs) with symmetry-tuned polarity and photocatalytic activity, *Angew. Chem. Int. Ed.* 59 (2020) 23845–23853.
- [28] S. Wei, F. Zhang, W. Zhang, P. Qiang, K. Yu, X. Fu, D. Wu, S. Bi, F. Zhang, Semiconducting 2D triazine-cored covalent organic frameworks with unsubstituted olefin linkages, *J. Am. Chem. Soc.* 141 (2019) 14272–14279.
- [29] S. Bi, C. Yang, W. Zhang, J. Xu, L. Liu, D. Wu, X. Wang, Y. Han, Q. Liang, F. Zhang, Two-dimensional semiconducting covalent organic frameworks via condensation at arylmethyl carbon atoms, *Nat. Commun.* 10 (2019) 2467.
- [30] F. Zhang, S. Wei, W. Wei, J. Zou, G. Gu, D. Wu, S. Bi, F. Zhang, Trimethyltriazine-derived olefin-linked covalent organic framework with ultralong nanofibers, *Sci. Bull.* 65 (2020) 1659–1666.
- [31] M. Winter, R.J. Brodd, What are batteries, fuel cells, and supercapacitors? *Chem. Rev.* 104 (2004) 4245–4270.
- [32] F. Cheng, J. Chen, Metal-air batteries: from oxygen reduction electrochemistry to cathode catalysts, *Chem. Soc. Rev.* 41 (2012) 2172–2192.

[33] M.K. Debe, Electrocatalyst approaches and challenges for automotive fuel cells, *Nature* 486 (2012) 43–51.

[34] S. Yang, Q. Cheng, J. Mao, Q. Xu, Y. Zhang, Y. Guo, T. Tan, W. Luo, H. Yang, Z. Jiang, Rational design of edges of covalent organic networks for catalyzing hydrogen peroxide production, *Appl. Catal. B* 298 (2021), 120605.

[35] M. Xiao, J. Zhu, L. Ma, Z. Jin, J. Ge, X. Deng, Y. Hou, Q. He, J. Li, Q. Jia, S. Mukerjee, R. Yang, Z. Jiang, D. Su, C. Liu, W. Xing, Microporous framework induced synthesis of single-atom dispersed Fe-N-C acidic ORR catalyst and its in situ reduced Fe-N4 active site identification revealed by X-ray absorption spectroscopy, *ACS Catal.* 8 (2018) 2824–2832.

[36] L. Xue, Y. Li, X. Liu, Q. Liu, J. Shang, H. Duan, L. Dai, J. Shui, Zigzag carbon as efficient and stable oxygen reduction electrocatalyst for proton exchange membrane fuel cells, *Nat. Commun.* 9 (2018) 3819.

[37] Y. Chen, S. Ji, C. Chen, Q. Peng, D. Wang, Y. Li, Single-atom catalysts: synthetic strategies and electrochemical applications, *Joule* 2 (2018) 1242–1264.

[38] B. Lu, Q. Liu, S. Chen, Electrocatalysis of single-atom sites: impacts of atomic coordination, *ACS Catal.* 10 (2020) 7584–7618.

[39] M.B. Gawande, P. Fornasiero, R. Zboril, Carbon-based single-atom catalysts for advanced applications, *ACS Catal.* 10 (2020) 2231–2259.

[40] A. Wang, J. Li, T. Zhang, Heterogeneous single-atom catalysis, *Nat. Rev. Chem.* 2 (2018) 65–81.

[41] S. Mitchell, J. Pérez-Ramírez, Atomically precise control in the design of low-nuclearity supported metal catalysts, *Nat. Rev. Mater.* 6 (2021) 969–985.

[42] S.K. Kaiser, Z. Chen, D. Faust Akl, S. Mitchell, J. Pérez-Ramírez, Single-atom catalysts across the periodic table, *Chem. Rev.* 120 (2020) 11703–11809.

[43] K. Yuan, D. Lützenkirchen-Hecht, L. Li, L. Shuai, Y. Li, R. Cao, M. Qiu, X. Zhuang, M.K.H. Leung, Y. Chen, U. Scherf, Boosting oxygen reduction of single iron active sites via geometric and electronic engineering: nitrogen and phosphorus dual coordination, *J. Am. Chem. Soc.* 142 (2020) 2404–2412.

[44] P. Yin, T. Yao, Y. Wu, L. Zheng, Y. Lin, W. Liu, H. Ju, J. Zhu, X. Hong, Z. Deng, G. Zhou, S. Wei, Y. Li, Single cobalt atoms with precise N-coordination as superior oxygen reduction reaction, *Catal. Angew. Chem. Int. Ed.* 55 (2016) 10800–10805.

[45] J. Yang, Z. Wang, C.X. Huang, Y. Zhang, Q. Zhang, C. Chen, J. Du, X. Zhou, Y. Zhang, H. Zhou, L. Wang, X. Zheng, L. Gu, L.M. Yang, Y. Wu, Compressive strain modulation of single iron sites on helical carbon support boosts electrocatalytic oxygen reduction, *Angew. Chem. Int. Ed.* 60 (2021) 22722–22728.

[46] X. Xie, C. He, B. Li, Y. He, D.A. Cullen, E.C. Wegener, A.J. Kropf, U. Martinez, Y. Cheng, M.H. Engelhard, M.E. Bowden, M. Song, T. Lemmon, X.S. Li, Z. Nie, J. Liu, D.J. Myers, P. Zelenay, G. Wang, G. Wu, V. Ramani, Y. Shao, Performance enhancement and degradation mechanism identification of a single-atom Co–N–C catalyst for proton exchange membrane fuel cells, *Nat. Catal.* 3 (2020) 1044–1054.

[47] H. Fei, J. Dong, Y. Feng, C.S. Allen, C. Wan, B. Voloskiy, M. Li, Z. Zhao, Y. Wang, H. Sun, P. An, W. Chen, Z. Guo, C. Lee, D. Chen, I. Shakir, M. Liu, T. Hu, Y. Li, A. I. Kirkland, X. Duan, Y. Huang, General synthesis and definitive structural identification of MN4C4 single-atom catalysts with tunable electrocatalytic activities, *Nat. Catal.* 1 (2018) 63–72.

[48] S. Liu, Z. Li, C. Wang, W. Tao, M. Huang, M. Zuo, Y. Yang, K. Yang, L. Zhang, S. Chen, P. Xu, Q. Chen, Turning main-group element magnesium into a highly active electrocatalyst for oxygen reduction reaction, *Nat. Commun.* 11 (2020) 938.

[49] S. Wei, Y. Wang, W. Chen, Z. Li, W.C. Cheong, Q. Zhang, Y. Gong, L. Gu, C. Chen, D. Wang, Q. Peng, Y. Li, Atomically dispersed Fe atoms anchored on COF-derived N-doped carbon nanospheres as efficient multi-functional catalysts, *Chem. Sci.* 11 (2019) 786–790.

[50] Q. Xu, H. Zhang, Y. Guo, J. Qian, S. Yang, D. Luo, P. Gao, D. Wu, X. Li, Z. Jiang, Y. Sun, Standing carbon-supported trace levels of metal derived from covalent organic framework for electrocatalysis, *Small* 15 (2019), e1905363.

[51] W. Zhou, H. Su, Y. Li, M. Liu, H. Zhang, X. Zhang, X. Sun, Y. Xu, Q. Liu, S. Wei, Identification of the evolving dynamics of coordination-unsaturated iron atomic active sites under reaction conditions, *ACS Energy Lett.* 6 (2021) 3359–3366.

[52] F. Kong, R. Si, N. Chen, Q. Wang, J. Li, G. Yin, M. Gu, J. Wang, L.-M. Liu, X. Sun, Origin of hetero-nuclear Au–Co dual atoms for efficient acidic oxygen reduction, *Appl. Catal. B* 301 (2022), 120782.

[53] Y. Li, B. Wei, M. Zhu, J. Chen, Q. Jiang, B. Yang, Y. Hou, L. Lei, Z. Li, R. Zhang, Y. Lu, Synergistic effect of atomically dispersed Ni–Zn pair sites for enhanced CO₂ electroreduction, *Adv. Mater.* 33 (2021), e2102212.

[54] L. Gong, H. Zhang, Y. Wang, E. Luo, K. Li, L. Gao, Y. Wang, Z. Wu, Z. Jin, J. Ge, Z. Jiang, C. Liu, W. Xing, Bridge bonded oxygen ligands between approximated FeN4 sites confer catalysts with high ORR performance, *Angew. Chem. Int. Ed.* 59 (2020) 13923–13928.

[55] T. Ding, X. Liu, Z. Tao, T. Liu, T. Chen, W. Zhang, X. Shen, D. Liu, S. Wang, B. Pang, D. Wu, L. Cao, L. Wang, T. Liu, Y. Li, H. Sheng, M. Zhu, T. Yao, Atomically precise dinuclear site active toward electrocatalytic CO₂ reduction, *J. Am. Chem. Soc.* 143 (2021) 11317–11324.

[56] M. Xiao, H. Zhang, Y. Chen, J. Zhu, L. Gao, Z. Jin, J. Ge, Z. Jiang, S. Chen, C. Liu, W. Xing, Identification of binuclear Co2N5 active sites for oxygen reduction reaction with more than one magnitude higher activity than single atom CoN4 site, *Nano Energy* 46 (2018) 396–403.

[57] M. Xiao, Y. Chen, J. Zhu, H. Zhang, X. Zhao, L. Gao, X. Wang, J. Zhao, J. Ge, Z. Jiang, S. Chen, C. Liu, W. Xing, Climbing the apex of the ORR volcano plot via binuclear site construction: electronic and geometric engineering, *J. Am. Chem. Soc.* 141 (2019) 17763–17770.

[58] Y. Yang, Y. Qian, H. Li, Z. Zhang, Y. Mu, D. Do, B. Zhou, J. Dong, W. Yan, Y. Qin, L. Fang, R. Feng, J. Zhou, P. Zhang, J. Dong, G. Yu, Y. Liu, X. Zhang, X. Fan, O-coordinated W–Mo dual-atom catalyst for pH-universal electrocatalytic hydrogen evolution, *Sci. Adv.*, 6 eaba 6586.

[59] V.N. Nemykin, D.E. Nevon, L.S. Ferch, M. Shepit, D.E. Herbert, J. van Lierop, Accurate prediction of mössbauer hyperfine parameters in bis-axially coordinated Iron(II) phthalocyanines using density functional theory calculations: a story of a single orbital revealed by natural bond orbital analysis, *Inorg. Chem.* 60 (2021) 3690–3706.

[60] Y. Pan, R. Lin, Y. Chen, S. Liu, W. Zhu, X. Cao, W. Chen, K. Wu, W.C. Cheong, Y. Wang, L. Zheng, J. Luo, Y. Lin, Y. Liu, C. Liu, J. Li, Q. Lu, X. Chen, D. Wang, Q. Peng, C. Chen, Y. Li, Design of single-atom Co-N5 catalytic site: a robust electrocatalyst for CO₂ reduction with nearly 100% CO selectivity and remarkable stability, *J. Am. Chem. Soc.* 140 (2018) 4218–4221.

[61] N. Zhang, T. Zhou, J. Ge, Y. Lin, Z. Du, Ca Zhong, W. Wang, Q. Jiao, R. Yuan, Y. Tian, W. Chu, C. Wu, Y. Xie, High-density planar-like Fe2N6 structure catalyzes efficient oxygen reduction, *Matter* 3 (2020) 509–521.

[62] F. de Groot, High-resolution X-ray emission and X-ray absorption spectroscopy, *Chem. Rev.* 101 (2001) 1779–1808.

[63] H.B. Yang, S.-F. Hung, S. Liu, K. Yuan, S. Miao, L. Zhang, X. Huang, H.-Y. Wang, W. Cai, R. Chen, J. Gao, X. Yang, W. Chen, Y. Huang, H.M. Chen, C.M. Li, T. Zhang, B. Liu, Atomically dispersed Ni(i) as the active site for electrochemical CO₂ reduction, *Nat. Energy* 3 (2018) 140–147.